Supplementary Information

The cohesive properties and pyrolysis mechanism of an aprotic ionic liquid tetrabutylammonium bis(trifluoromethanesulfonyl)imide

Shijie Liu,[a] Runhong Wei,[b] Guangjun Ma,[c] Ailin Li,[d] Olaf Conrad,[e] Jiangshui Luo[a,*]

[a]Lab of Electrolytes and Phase Change Materials, College of Materials Science and Engineering, Sichuan University, Chengdu 610065, China.

[b]Fujian Ningde Aishuyuncheng New Materials Technology Co., Ltd., Ningde 355200, China

[c]Chengdu Weilai Engineering Technology Co., Ltd, No. 366 North Section of Hupan Road, Zhengxing Street, Tianfu New District, Chengdu 610299, China

[d]College of Science, Civil Aviation University of China, Tianjin 300300, China

[e]Pajarito Powder LLC, 3600 Osuna Rd, Albuquerque, NM 87109, USA

Contents

1 Infrared vibration assignments

Figure S1 presents the ATR-IR spectra of $[N_{4444}][NTf_2]$, the peaks at 2971, 2879, 1477 and 884 cm^{-1} are attributed to the tetrabutylammonium cations,[1, 2] while the peaks at 1352, 1227, 1184, 1134, 794, 762, 739, 610, 567 and 511 cm^{-1} are associated with the bis(trifluoromethanesulfonyl)imide anions.[2-6] All frequencies described in IR of $[N_{4444}]^+$ cation and $[NTf_2]^-$ anion are summarized in **Table S1**.

The peaks for the cation part are distinguished, focusing between 2971 and 1477 cm^{-1}, which are attributed to the stretching/bending vibrations of the $-CH_3$ and $-CH_2$ groups. Note that the new band at 884 cm^{-1} could be associated with the butyl chain stretching vibration of $[N_{4444}]^+$ cation. In the part of anion, the characteristic frequencies between 1352 and 511 cm^{-1} describe the stretching and bending vibrations of $-SO_2$, $-CF_3$, S-N-S and C-S bonds of $[NTf_2]^-$ anion.

2 Nuclear magnetic resonance (NMR) results

Figure S2 shows the ^1H NMR and ^{13}C NMR spectrums of $[N_{4444}][NTf_2]$. The characterization agrees well with the reported NMR spectra in literature.[2, 7] The chemical shifts are shown as follows: δ_H (400 MHz,

DMSO-*d*6, δ/ppm): 3.20–3.12 (m, 8H, N-CH_2), 1.63–1.50 (m, 8H, NCH_2-CH_2), 1.31 (h, J = 7.4 Hz, 8H, NCH_2CH_2-CH_2), 0.93 (t, J = 7.3 Hz, 12H, CH_2-CH_3); δ_C (101 MHz, DMSO-*d*6, δ/ppm): 117.90, 57.55, 57.52, 23.05, 19.20, 13.47.

3 XRD analysis

Figure. S3 shows the XRD pattern of $[N_{4444}][NTf_2]$ at 25°C. Prominent diffractive peaks can correspond to that indexed to standard pure $[N_{4444}][NTf_2]$ with monoclinic phase structures (CCDC No.1432362, lattice parameters, a = 1.331 nm, b = 2.900 nm, c = 1.352 nm and β = 94.059°; V_{cell} = 5.21 nm^3, Z = 8; space group, P1 12 1(4)) at −173.15°C. New peaks appear at the 2θ of 25.4, 26.5, 27.9, 29.3, 30.8, 33.1 and 34.9°, while the peaks at 2θ of 6.1, 6.5 and 7.3° disappeared. The new peaks reveal that the phase structures of $[N_{4444}][NTf_2]$ have some changes in the temperatures range of −173.15°C to 25°C.

4 Phase transition

During the heating or cooling scan in the differential scanning calorimetry (DSC) measurements recorded at 10°C min^{-1}, the fusion and solidification process of $[N_{4444}][NTf_2]$ was observed at 90.8 and 73.1°C, respectively, with the supercooling of 17.7°C. Moreover, the molar enthalpy of fusion (ΔH_{fusion}) and solidification (ΔH_{cr}) is 23.3 and −23.0 kJ mol^{-1}, respectively. The specific fusion enthalpy and fusion enthalpy per unit volume are 42.9 J g^{-1} and 57.2 MJ m^{-3}, respectively.

5 Heat capacity

The dependence of solid and liquid-state heat capacities ($C_{p,\,s}$ and $C_{p,\,l}$) on temperatures is described as polynomial equation.

$$C_P = a_0 + a_1 T + a_2 T^2 \quad \text{(S1)}$$

For the ideal gaseous phase of $[N_{4444}][NTf_2]$, the $C_{p,\,g}$ can be considered as the sum of contribution from the heat capacities of cation and anion.[8] The $C_{p,\,g}$ of $[NTf_2]^-$ from −173.15 to 726.85 °C is known,[9] while the $C_{p,\,g}$ of $[N_{4444}]^+$ can be estimated by the Joback group contribution method (Eq S2).[10]

$$C_p(T) = \left(\sum_i n_i A_{Cpi} - 37.93\right) + \left(\sum_i n_i B_{Cpi} + 0.210\right)T + \left(\sum_i n_i C_{Cpi} - 3.91\times10^{-4}\right)T^2 + \left(\sum_i n_i D_{Cpi} + 2.07\times10^{-7}\right)T^3 \quad \text{(S2)}$$

where the A_{Cpi}, B_{Cpi}, C_{Cpi} and D_{Cpi} are group contribution parameters; n_i is the numbers of groups for type i. It mentioned that the parameters of the -CH_2 group were modified by the increment of the reported standard $C_{p,\,g}$ data of rising branches (n_i = 0–3) of tetraalkylammonium cation at 25°C. [11, 12] Finally, the summation of the contribution of cation and anion, $C_{p,\,g}$ can also be fitted by polynomial regression.

The raw data of $C_{p,\,s}$ and $C_{p,\,l}$ of $[N_{4444}][NTf_2]$ are presented in **Figure. S4.** The modified parameters of -CH_2 group is shown in **Table S2**. The results of $C_{p,\,s}$, $C_{p,\,l}$ and $C_{p,\,g}$ by polynomial fitting were listed in **Table S3**. It shows that the $C_{p,\,l}$ of $[N_{4444}][NTf_2]$ exceed 1000 J K^{-1} mol^{-1} at the temperature higher than 110 °C, emphasizing the potential to a new heat storage material.

6 Vaporization enthalpy and vapor pressure

The reorganized form of the Langmuir equation (Eq S3) can describe the linear evaporative mass loss of ILs and low volatile matter:

$$P_{vap} = k_{vap} \cdot v \quad \text{(S3)}$$

where:

$$k_{vap} = (2\pi R)^{0.5}/\alpha_{vap}\; v = (1/a)|dm/dt|\left(T/M_W\right)^{0.5} \quad \text{(S4)}$$

the P_{vap} is vapor pressure, k_{vap} is the vaporization coefficient and α_{vap} is the vaporization constant; $(1/a)|dm/dt|$ is the absolute value of weight loss rate per unit area at the interface of the crucible and

the M_W is the molar weight of the sample. The value of k_{vap} is relevant to the experimental condition (instrument and atmosphere) rather than the investigated sample and temperature range.[13] Thus, it can be obtained through the IGA experiments of known-vapor-pressure standard compounds.

To quantitatively analyze the ΔH_{vap} of $[N_{4444}][NTf_2]$, we follow the isothermalgravimetric analysis (IGA) method developed by H. Luo.[14]

$$\ln\left(T^{0.5}\left|\frac{dm}{dt}\right|\right) = c' - \Delta H_{vap}/(RT) \quad \text{(S5)}$$

Eq S5 is a basement for the calculation of ΔH_{vap} by IGA experiments, where the $\Delta H_{vap}(T_a)$ can be derived by the slope of a plot of $\ln(T^{0.5}|dm/dt|)$ versus $1000T^{-1}$ (at least three elevated temperatures).

The trends of weight loss of Glycerol and $[N_{4444}][NTf_2]$ during IGA measurements is rigorously linear with a correlation coefficient R^2 exceeding 0.998 (**Figure S5a** and **S6a**), emphasizing that its vaporization process is the zero-order reaction. The weight loss rate and corresponding R^2 at different temperatures are listed in **Table S6**. $[N_{4444}][NTf_2]$ exhibits very low volatility (ΔH_{vap} = 144.2 kJ mol^{-1}) even at 295°C (**Figure S5b** and **Table S5)**. By transformation from liquid to solid range, the ΔH_{vap}, ΔH_{sub} and corresponding E_{coh} were obtained (**Table S8**). It shows that the E_{coh} increases with reduced temperature. The $E_{coh} = -\Delta U_{vap}$ or $-\Delta U_{sub}$ reveals the potential energy of the condensed matter. Thus, the sudden jump of E_{coh} corresponds to the phase change, indicating that the potential energy transfers to more negative region.

The value of k_{vap} is 1748.76 ± 72.92 Pa min cm^2 mg$^{-0.5}$ mol$^{-0.5}$ K$^{-0.5}$ calculated by the vapor pressure (P_{vap}) data of glycerol[15] **(Figure S5b)**. The P_{vap} of $[N_{4444}][NTf_2]$ are listed in **Table S9**, which range from 0.02 to 146 Pa in the temperature range of 230 to 350 °C. The Antoine equation is used in this work to determine the correlation between P_{vap} and temperatures. It can be written as:

$$lgP = A - B/(T + C) \quad \text{(S6)}$$

where the A, B and C are dimensionless empirical Antoine constants at given temperatures range. The multiple linear regression of the obtained data shows that A, B and C are 19.01, 15440.52 and 241.73, respectively. **Figure S6**c presents the experimental P_{vap} and those calculated P_{vap} by Antoine equation, as a function of temperatures. Compared to the values of experimental P_{vap}, the calculated ones reflect a 4.75% absolute average derivation. The calculated A, B and C of are $[C_2mim][NTf_2]$ are 7.69, −141.26 and 2997.22, respectively, while A, B and C of $[C_4mim][NTf_2]$ are 5.70, 4360.02 and 229.68, respectively.

7 Lattice energy

The lattice potential energy of solid-state ionic liquids (U_L) includes the electrostatic interaction energy (E_{es}) and short-range interaction energy (E_{SR}). The short-range interaction includes several components, such as π-π interactions, hydrogen bonding and van der Waals interactions.

$$U_L = E_{es} + E_{SR} \tag{S7}$$

However, in the case of aprotic ILs without N-containing heterocyclic compounds, the π-π interactions are not considered. Moreover, the contributions of the van der Waals interaction on U_L is only about 1% for the simple ionic solid[16], hence the U_L of solid state of aprotic ILs can be approximated to its electrostatic part E_{es}. Madelung[17] summed the total electrostatic interaction energy in the crystal structure as:

$$E_{es} = -\frac{M|Z_+||Z_-|e^2}{4\pi\varepsilon_0 r_{min}} \tag{S8}$$

where the Z_+ and Z_- is the charge of the cation and anion, respectively, r_{min} is the distance to the nearest counterion, e is the element charge (1.602×10^{-19} C), M is the Madelung constant and ε_0 is the vacuum permittivity (8.854×10^{-12} F m^{-1}). The Madelung constant and lattice energy ΔU_L was calculated by the expanding unit-cell generalized numerical (EUGEN) method[18] based on the reported crystal structure of $[N_{4444}][NTf_2]$.[7]

The unit cell structure and the equilibrium geometries of ions in the crystalline $[N_{4444}][NTf_2]$ shows that the cation has a highly symmetrical structure, illustrating that the van der Waals forces between cations are feeble. Besides, the electrostatic potential map reveals that the negative charge is partially distributed on the oxygen atoms in the anion, while the positive charge distributions concentrate on the nitrogen atoms of $[N_{4444}]^+$, making the strength of possible *H*-bonds negligible. Therefore, the lattice energy can be approximated to the electrostatic interactions energy between the $[N_{4444}]^+$ and $[NTf_2]^-$. From the crystal structure data of $[N_{4444}][NTf_2]$ at −173.15 °C, the minimum distance between the cation and anion (r_{min}) is 0.410 nm, the density (ρ) is 1.33 g cm^{-1}, the Madelung constant of $[N_{4444}][NTf_2]$ is 1.205, the lattice potential energy U_L is −408.3 kJ mol^{-1} and the dipole moment of unit cell is 29.53 Debye by EUGEN method.

8 Pyrolysis kinetic analysis

The pyrolysis process of ILs is generally assumed as follows:

$$Ionicliquid \xrightarrow{k} Volatiles + Char \tag{S9}$$

where volatiles and *k* indicate the volatile degradation product and reaction constant, respectively. The dependence of *k* on temperature can be described as the Arrhenius equation (Eq S10):

$$k = Ae^{-\frac{E_a}{RT}} \tag{S10}$$

where A and E_a represent the pre-exponential factor (min^{-1}) and activation energy (kJ mol^{-1}), respectively. The reaction rate of the condensed state is generally presented in the following form:

$$\frac{d\alpha}{dt} = kf(\alpha) \tag{S11}$$

where α, t and $f(\alpha)$ indicates the degree of conversion from reactants to products, taken time and the function of conversion degree (Eq S12), respectively. The function $f(\alpha)$ is dependent on the

reaction mechanism and *n* is the kinetic (Avrami) exponent. The α terms normalized weight loss during thermal degradation as Eq S13:

$$f(\alpha) = (1-\alpha)^n \tag{S12}$$

$$\alpha = \frac{m_i - m_\alpha}{m_i - m_f} \tag{S13}$$

where m_i, m_α and m_f represent the initial weight, weight at conversion α and final weight after decomposition of sample, respectively. Eq S14, formed by combining the Eqs S10, S11 and S12, is a primary equation for calculating of kinetic parameters based on TG data.

$$\frac{d\alpha}{dt} = A \cdot (1-\alpha)^n \cdot e^{-\frac{E_a}{RT}} \tag{S14}$$

For the ramped TGA, the temperature increases linearly with time in constant heating rate β_H:

$$\frac{dT}{dt} = \beta_H \tag{S15}$$

Thus, the Eq S14 can be rewritten as:

$$\frac{d\alpha}{dT} = \frac{A}{\beta_H} \cdot (1-\alpha)^n \cdot e^{-\frac{E_a}{RT}} \tag{S16}$$

This equation expresses the fraction of sample converted as function of temperature change. The kinetic parameters can be calculated by differential and integral methods.

8.1 Differential method

In this work, the kinetic parameters were calculated by the most prominent Ozawa,[19] Kissinger[20] and Starink[21] differential methods, respectively, which use the peak temperature of DTG data to derive the activation energy and pre-exponential factor. They are based on Eq S17, S18 and S19, respectively, where the T_p is the peak temperature of the DTG curve and G(α) is the integral form of Eq S16, associated with the reaction mechanism.

$$\ln(\beta_H) = \ln\left(\frac{0.048AE_a}{RG(\alpha)}\right) - 1.0516\frac{E_a}{RT_p} \quad \text{(S17)}$$

$$\ln\left(\frac{\beta_H}{T_p^{\,2}}\right) = \ln\left(\frac{AR}{E_a G(\alpha)}\right) - \frac{E_a}{RT_p} \quad \text{(S18)}$$

$$\ln\left(\frac{\beta_H}{T_p^{\,1.92}}\right) = \ln\left(\frac{AR^{0.92}}{E_a{}^{0.92} G(\alpha)}\right) - 0.312 - 1.008\frac{E_a}{RT_p} \quad \text{(S19)}$$

$$G(\alpha) = \int_0^{\alpha} \frac{\mathrm{d}\alpha}{(1-\alpha)^n} = \frac{AE_a}{\beta_H R}\int_{\infty}^{u} \frac{e^{-u}}{u^2}\mathrm{d}u \quad \text{(S20)}$$

The activation energies E_a can be calculated by the slope of a plot $\ln(\beta_H)$, $\ln(\beta_H T^{-2})$, $\ln(\beta_H T^{-1.92})$ against $1000T^{-1}$ for several experiments at different heating rates (at least three). The value of E_a and intercept are necessary for the calculation of the kinetic (Avrami) exponent n of reaction (Eq S21),[22]

$$n = \left(1-\alpha_p\right)E_a \exp(\text{constant})\frac{\exp(-E_a / RT_p)}{\beta_H R(\mathrm{d}\alpha_p / \mathrm{d}T)} \quad \text{(S21)}$$

where the α_p and constant denote the fraction of conversion at peak temperature and value of intercept of Kissinger plot, respectively.

The pyrolysis process is assumed as reactions experienced with the formation of transition state. The pre-exponential factor A and other thermodynamic parameters such as enthalpy (ΔH), Gibbs energy (ΔG) and entropy (ΔS) change during the formation of the transition state can be derived by Eq S22–25 using the as-calculated activation energy:[23]

$$A = \frac{\beta_H E_a}{RT^2}\exp\left(\frac{E_a}{RT}\right) \quad \text{(S22)}$$

$$\Delta H = E_a - RT \quad \text{(S23)}$$

$$\Delta G = E_a + RT\ln\left(\frac{k_B T}{hA}\right) \quad \text{(S24)}$$

$$\Delta S = \frac{\Delta H - \Delta G}{T} \quad \text{(S25)}$$

where k_B is the Boltzmann constant (1.381×10^{-23} J K^{-1}) and h is the Plank constant (6.626×10^{-34} J s). This work used the intermediate value of heating rate β_H and corresponding characteristic temperatures to calculate the kinetic parameters.

Hence, by applying the Arrhenius equation with known kinetic parameters and as-calculated kinetic exponent, one can derive the reaction constant k at different temperatures and the corresponding half-life ($t_{1/2}$) which is the required time for half of material to degrade.

The heating rates can affect the heating efficiency and heating time of the sample, hence the TG curves and peak positions of DTG curves.[24] **Figure S7**a presents the TG-DTG curves of $[N_{4444}][NTf_2]$ from 25 to 600°C in nitrogen atmosphere at a heating rates of 5, 10 and 15 °C min^{-1}, respectively. It shows that the samples have completely degraded (mass loss of 100%) in the temperature range of 414 to 440 °C. The TG curves present an almost parallel shift towards higher temperatures with increasing heating rates, demonstrating that $[N_{4444}][NTf_2]$ is more stable at faster heating rates.

On the other hand, the heating rates also affect the peak positions of DTG curves. **Table S16** shows the onset temperatures (T_{onset}) and peak temperatures (T_p) of DTG curves for $[N_{4444}][NTf_2]$. The T_p at 5 °C min^{-1} was 402.3 °C shifted from to 412.1 and 419 at 10 and 15 °C min^{-1}, respectively, making the maximum temperature difference of more than 16 °C. Similar phenomena are observed in the T_{onset}, resulting in a difference of about 14 °C on onset temperatures between 5 and 15 °C min^{-1}. This dependence of characteristic temperatures (P) on heating rates (β_H) can be described as polynomial law:

$$P = B + C\beta_H + D\beta_H^{\,2} \quad \text{(S26)}$$

where both B, C and D are constants. By the polynomials fitting, the onset temperature T_{onset} and peak temperature T_p at 0 °C min^{-1} are 368.5 and 391.1 °C, respectively, with an exceptional high correlation R^2 of 0.99999.

Furthermore, as aforementioned methods, the shifts of T_p in DTG curves can be used to calculate the kinetics parameters of thermal degradation. The plots $\ln(\beta_H)$, $\ln(\beta_H T^{-2})$ and $\ln(\beta_H T^{-1.92})$ against $1000T^{-1}$ of $[N_{4444}][NTf_2]$, according to Eq S17, S18 and S19, are shown in **Figure S9b**. It infers that the activation energies (E_a) of $[N_{4444}][NTf_2]$ were 244.3, 241.9 and 244.0 kJ mol^{-1}, through Ozawa, Kissinger and Starink methods, respectively. Such a high value of E_a emphasizes the extremely high thermal stability of $[N_{4444}][NTf_2]$.

The intermediate β_H (10°C min^{-1}) and corresponding T_p (412.2°C) are used to determine the pre-exponential factors (A), as well as the activation enthalpy (ΔH), Gibbs energy (ΔG) and entropy (ΔS) during the formation of activated complex, by Eqs S22–S25.

The ΔG reveals the total energy increases of the system during the transform from the reagents to activated complex. The ΔH represents the energy difference between the reagent and the activated complex, which indicates the energy barrier to the formation of the transition state. The formation process could be restricted if the difference is large because the energy barrier is too high. In this work, such high ΔH = 237.4 kJ mol^{-1} highlights that the formation of the transition state has a high energy barrier during the thermal degradation of $[N_{4444}][NTf_2]$. The ΔS reflects how near the transition state is to its own thermodynamic equilibrium. The low entropy change, ΔS, implies that the material may pass through chemical or physical ageing process by bringing it to a transition state near its own thermodynamic equilibrium state. In this case, the sample shows little reactivity, resulting slow rate of reaction to form the activated complex.[25] On the other hand, a high ΔS means that the state is far from its thermodynamic equilibrium. Thus, the material's

reactivity is high and the formation of the activated complex can be faster resulting in a shorter reaction time. The value of ΔS of $[N_{4444}][NTf_2]$ is minimal compared with its ΔH. Therefore, it can be postulated that the transition state of $[N_{4444}][NTf_2]$ is close to its thermodynamic equilibrium, which leads to little reactivity. On the other hand, the positive ΔS also illustrates that the activated complex of $[N_{4444}][NTf_2]$ is more disordered than the initial substance.

Furthermore, from Eq 24, the kinetic exponent n is 0.005 which is very close to zero, illustrating that the pyrolysis of $[N_{4444}][NTf_2]$ is a zero-order reaction. Thus, taking the conversion function $f(\alpha)$ as unity, the half-life can be estimated from the Arrhenius equation. **Table S17** presents the half-life ($t_{1/2}$) in the temperature range of 330 to 440°C of $[N_{4444}][NTf_2]$. It shows that the $t_{1/2}$ reduces with increasing temperatures, emphasizing that higher temperature can facilitate thermal degradation.

8.2 Integral method

The integral methods are based on the TG curves data. The principle of these methods is that the temperature of conversion varies with the change in heating rate. Consequently, when samples run at several heating rates, the kinetic parameters of each conversion (α) during degradation can be calculated using the dependence of conversional temperatures against β_H. The methods contain Flynn-Wall-Ozawa (ASTM E-1641), Kissinger–Akahira–Sunose (KAS) and Starink methods.[26] The E_a at different α can be obtained from the plot of $\ln(\beta_H)$, $\ln(\beta_H T^{-2})$, $\ln(\beta_H T^{-1.92})$ versus $1000T^{-1}$ by Eq S27, 28 and 29, respectively.[24]

$$\ln(\beta_H) = \ln\left(\frac{0.048 A E_a}{R G(\alpha)}\right) - 1.052\frac{E_a}{R T_\alpha} \quad \text{(S27)}$$

$$\ln\left(\frac{\beta_H}{T_\alpha^{\ 2}}\right) = \ln\left(\frac{AR}{E_a G(\alpha)}\right) - \frac{E_a}{R T_\alpha} \quad \text{(S28)}$$

$$\ln(\frac{\beta_H}{T_\alpha^{1.92}}) = \ln\left(\frac{AR^{0.92}}{E_a^{0.92}G(\alpha)}\right) - 0.312 - 1.008\frac{E_a}{RT_\alpha} \quad \text{(S29)}$$

Figure S8 presents the conversion plots of $\ln(\beta_H)$, $\ln(\beta_H T^{-2})$, $\ln(\beta_H T^{-1.92})$ against 1000 T^{-1} of $[N_{4444}][NTf_2]$, in accordance with FWO, KAS and Starink methods, respectively. The plots for the 5−90% conversion range are used to derive the kinetic parameters of different temperatures. The E_a at different α with corresponding R^2 are listed in **Table S18**.

E_a's dependence not only reveals the complexity of the reaction process but also identifies the kinetic scheme. A uniform trend in the plot of E_a versus α implies that a single-step reaction occurs, while the apparent variations of E_a reflect that the reaction is a multiple-step process. It shows that the activation energy reduces with increasing temperature and tends to be flat on the 70% conversion, thus the thermal degradation of $[N_{4444}][NTf_2]$ is a multiple-step process. By the nonlinear fitting of the curve in **Figure 9**, the maximum and minimum value of E_a is 416.5 and 259.3 kJ mol^{-1}.

Furthermore, the decreasing dependency of activation energy on conversion attributes to the kinetic scheme of an endothermic reversible reaction followed by an irreversible one.[27] The process is like two consecutive steps A ↔ B → P. Supposing that irreversible reaction is the limiting step and the reversible reaction proceeds when the condition of the equilibrium constant K << 1 is fulfilled, thus the apparent activation energy E_a can be described as follows:[28]

$$E_a = E_2 + \Delta H^0 \quad \text{(S30)}$$

where the E_2 denotes the activation energy of irreversible reaction and the ΔH^0 is enthalpy of the reversible reaction, equal to the activation energy difference between direct and reverse reaction (E^+ and E^-). Therefore, the maximum E_a = 416.5 kJ mol^{-1} in all conversions indicates the sum of the E_a of irreversible reaction and the ΔH^0 of reversible reaction. At higher temperatures, for an

endothermic reaction, the reversible reaction transforms into an irreversible one due to the condition $K_1 >> 1$. Hence the minimum E_a = 259.3 kJ mol^{-1} approaches the activation energy value of irreversible reaction alone.

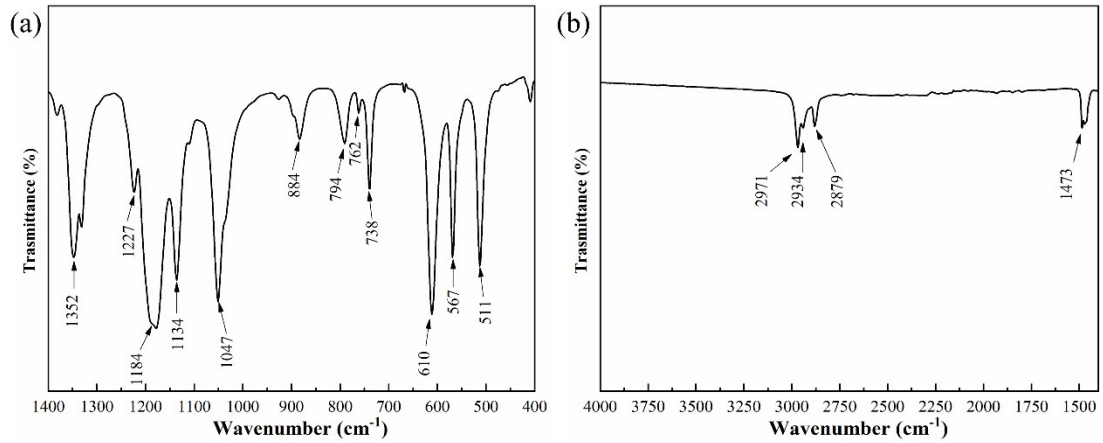

Figure S1. IR spectra of $[N_{4444}][NTf_2]$ in the special ranges of 1400 to 400 cm^{-1} (a) and 4000 to 1400 cm^{-1} (b), respectively.

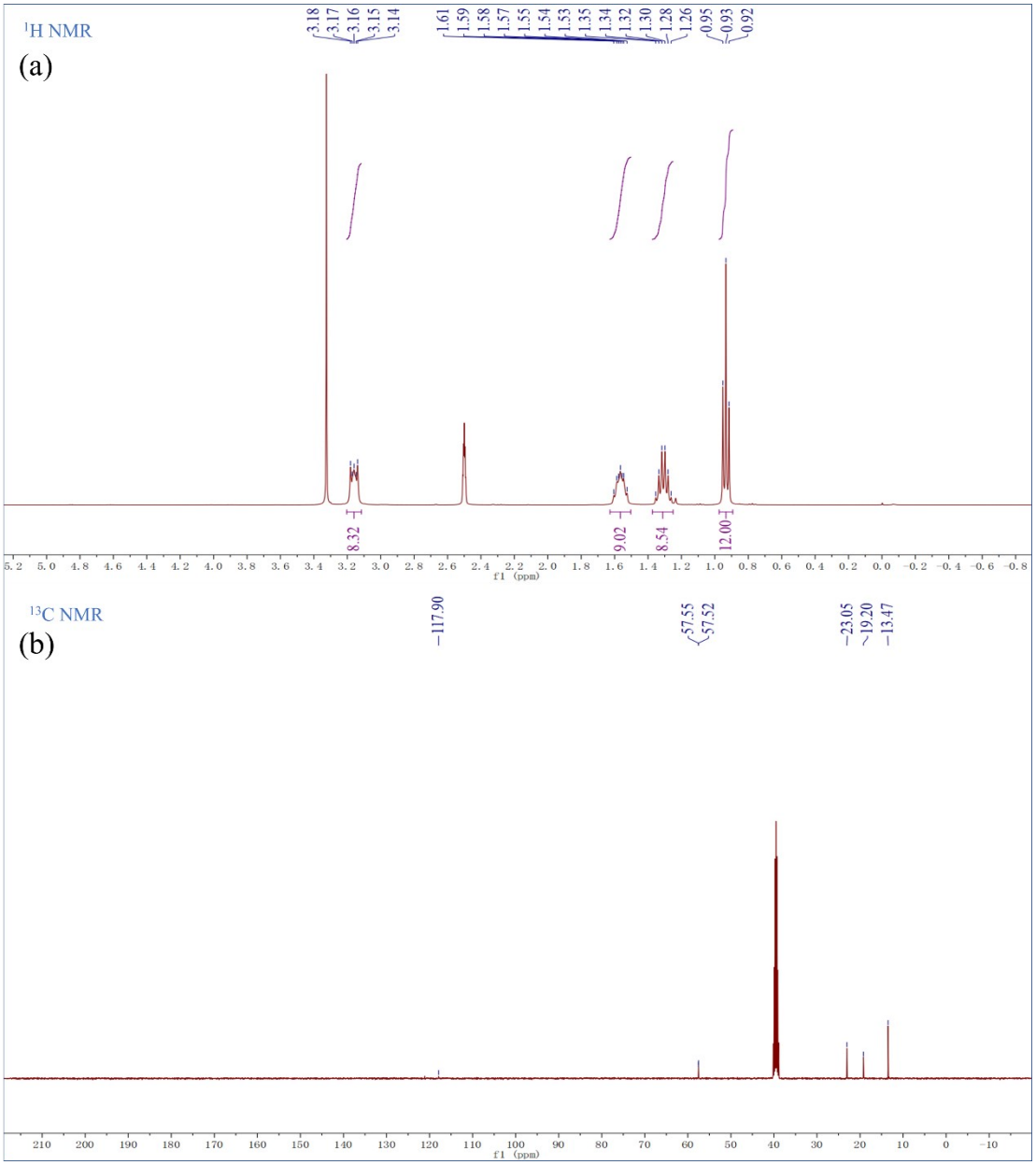

Figure S2. ^{1}H NMR and ^{13}C NMR spectra of [N_{4444}][NTf_2]. ^{1}H NMR (400 MHz, DMSO-d_6) δ 3.20 – 3.12 (m, 8H, N-CH_2), 1.63 – 1.50 (m, 8H, NCH_2-CH_2), 1.31 (h, J = 7.4 Hz, 8H, NCH_2CH_2-CH_2), 0.93 (t, J = 7.3 Hz, 12H, CH_2-CH_3) ppm. ^{13}C NMR (101 MHz, DMSO-d_6) δ 117.90, 57.55, 57.52, 23.05, 19.20, 13.47 ppm.

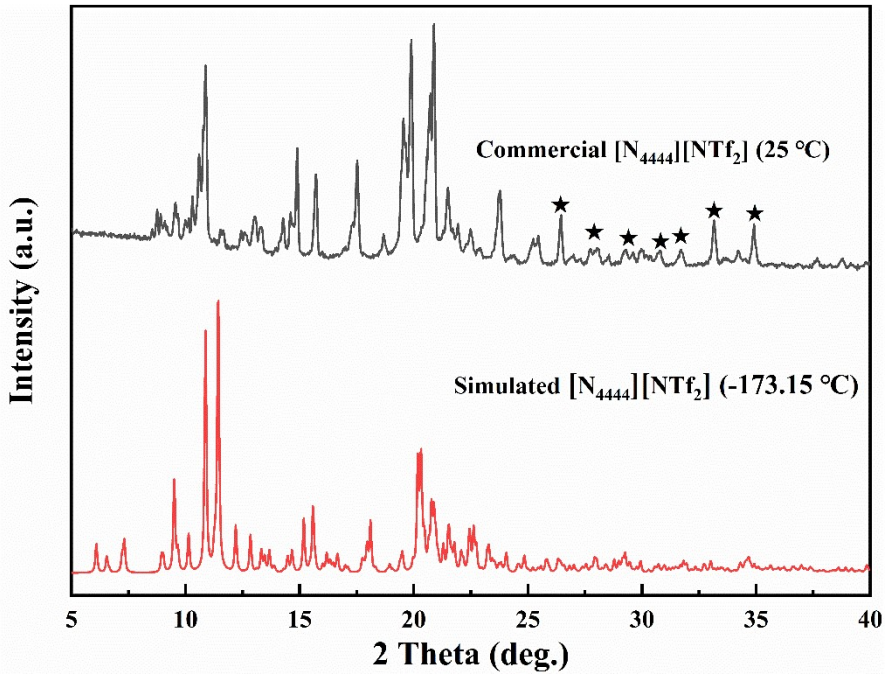

Figure S3. Comparison of the experimental powder XRD pattern of $[N_{4444}][NTf_2]$ at 25°C (upper) with simulated from crystal data determined at −173.15°C (bottom).

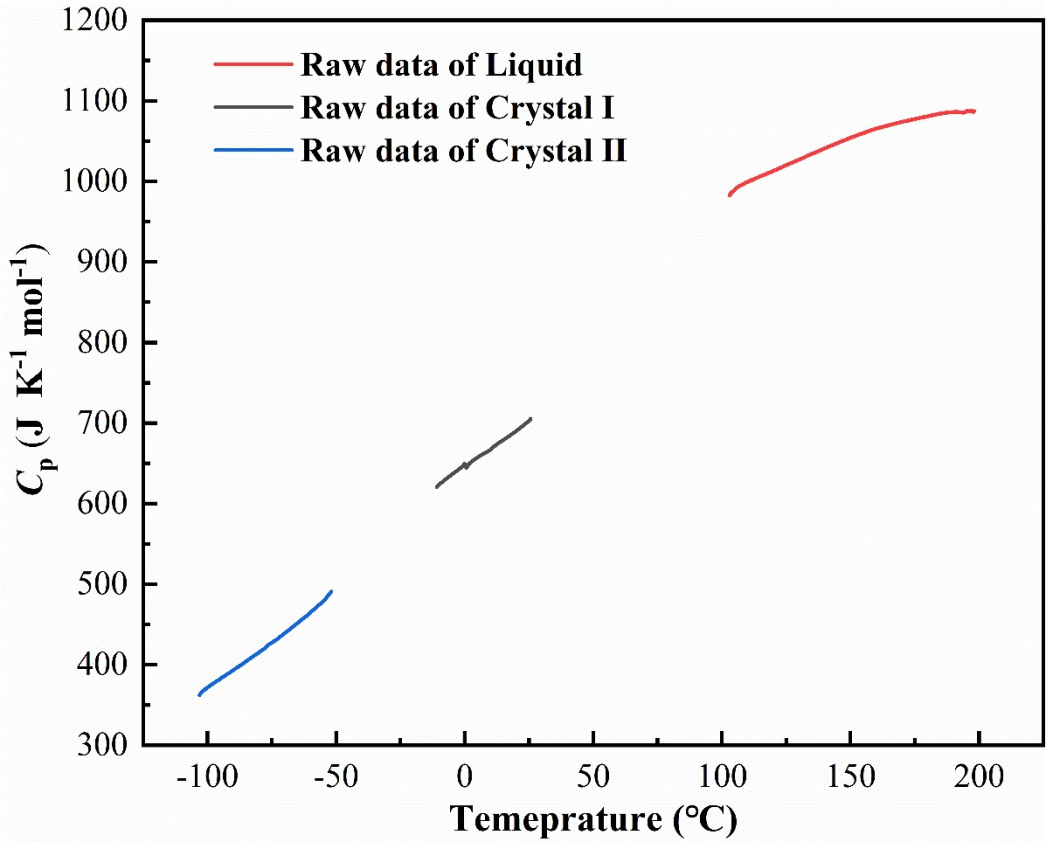

Figure S4. Raw data of Heat capacities of solid and liquid phases of $[N_{4444}][NTf_2]$.

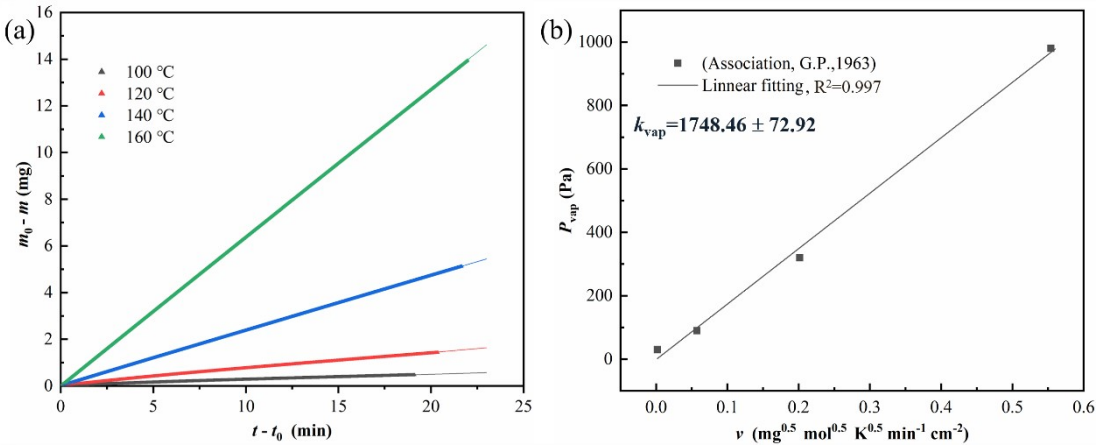

Figure S5. The plot of mass variation with time (a) and of P_{vap} versus v (b) of glycerol.

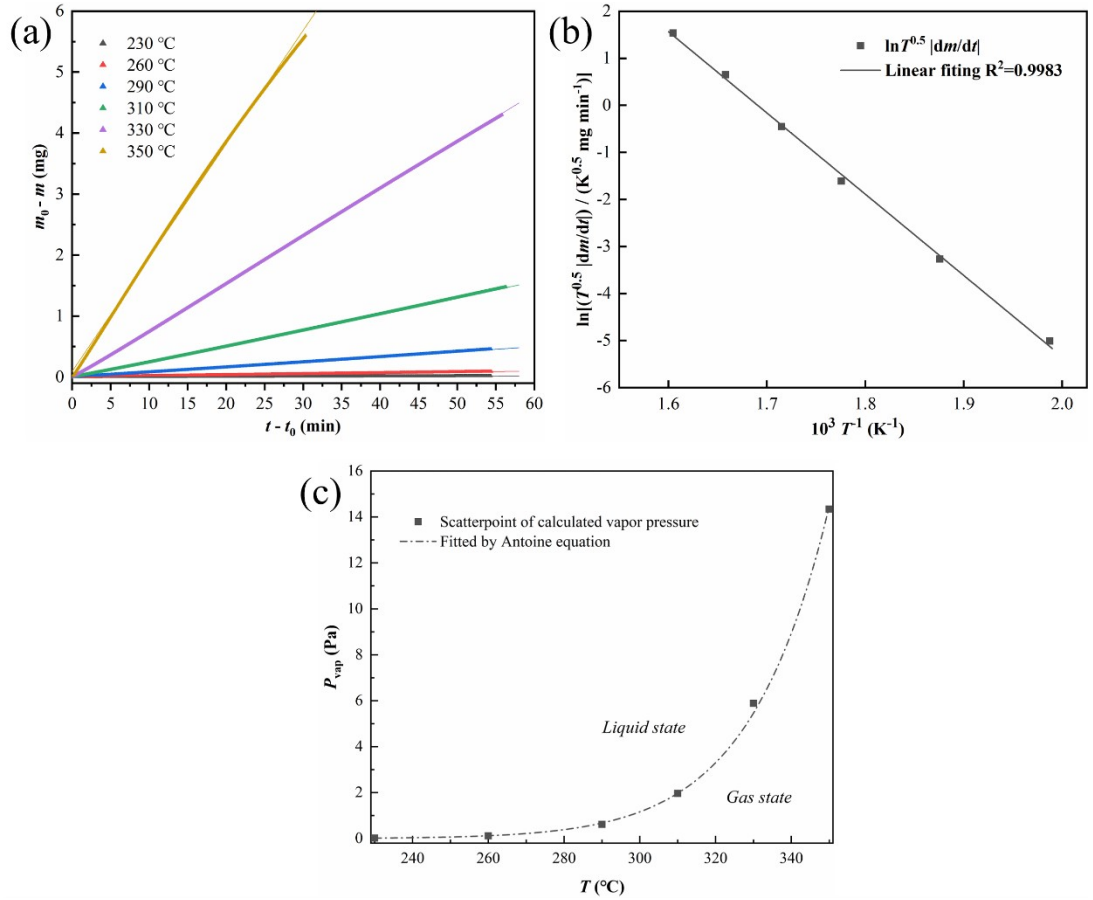

Figure S6. The plot of weight variation with time (a), ln($T^{0.5}$|dm/dt|) versus 10^3 T^{-1} (b) and vapor pressures P_{vap} versus temperatures of [N_{4444}][NTf_2] (c).

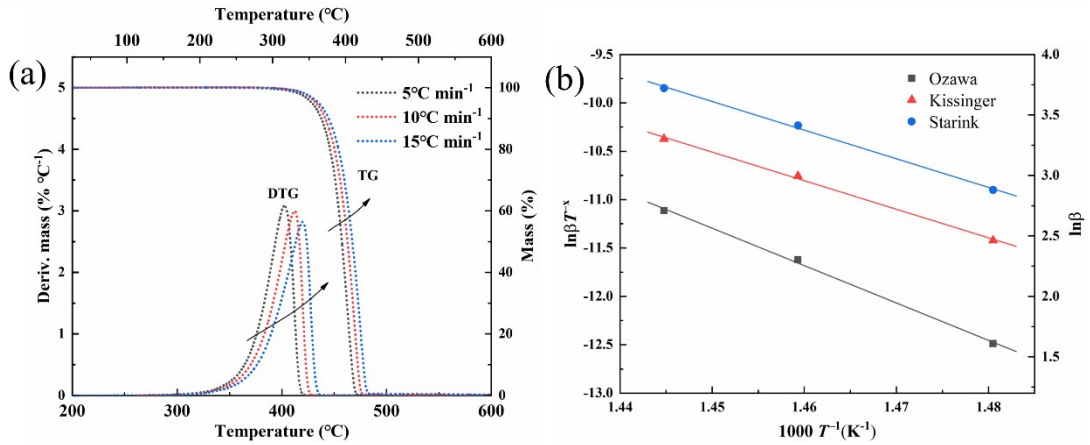

Figure S7. TG-DTG curves of $[N_{4444}][NTf_2]$ at heating rates of 5, 10 and 15°C min^{-1}, respectively (a); DTG kinetics of $[N_{4444}][NTf_2]$ by Ozawa, Kissinger and Starink methods, respectively (b).

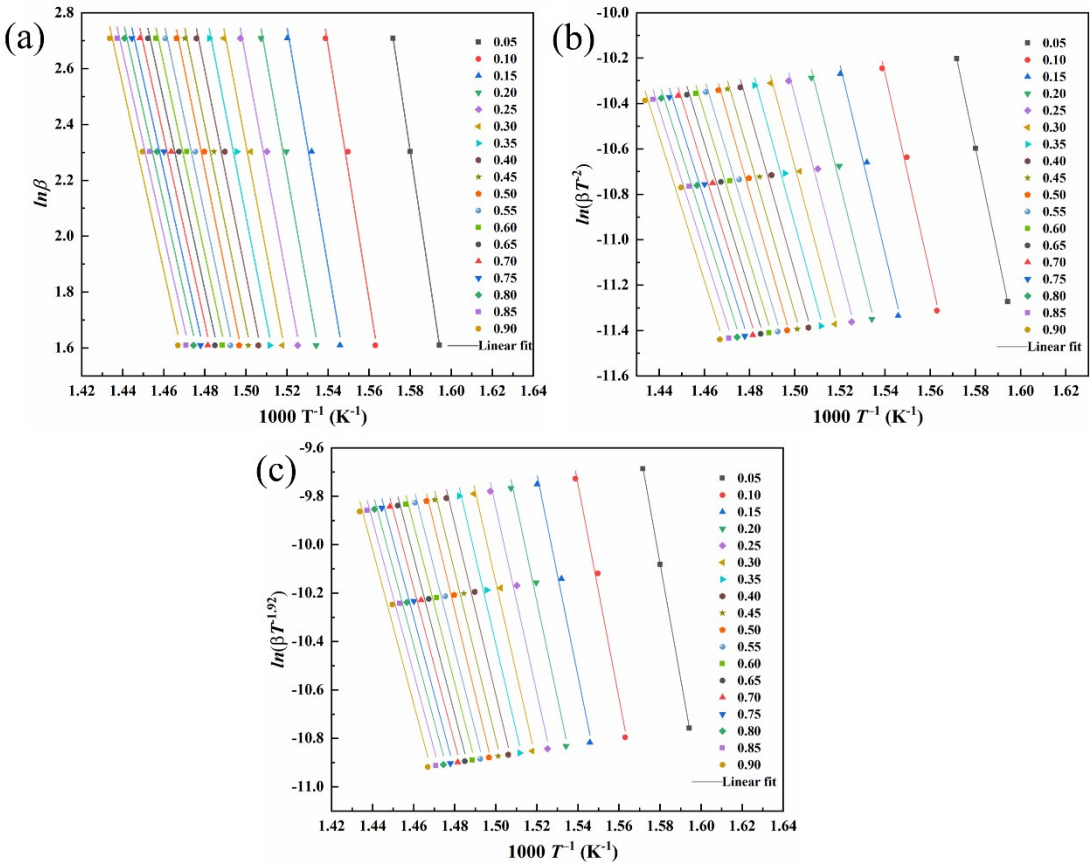

Figure S8. TG kinetics of $[N_{4444}][NTf_2]$ at different degree of conversion, by FWO method (a), KAS method (b) and Starink method (c).

Table S1. Observed IR bands of $[N_{4444}][NTf_2]$ and theirs assignments: sym, symmetric; asym, asymmetric; str, stretching vibration; ben, bending vibration.

Assignments	**Wavenumber (cm^{-1})**	**Reference**
CH_3 asym str, C-H str	2971	1,2
CH_2 asym str	2934	1,2
CH_3 sym str, C-H str	2879	1,2
CH_3 asym ben	1473	2
SO_2 asym str	1352	2-4
CF_3 sym str	1227	2-4
CF_3 asym str	1184	2-4
SO_2 sym str	1134	3,4
SNS asym str, C-N str	1047	1-4
Butyl chain str	884	3,4
C-S str	794	3,4
SNS sym str	762	3,4
CF_3 sym ben	739	3,4
SO_2 asym ben	610	3,4
CF_3 asym ben	567	5,6
CF_3 asym ben	511	6

Table S2. The modified parameters of -CH_2 group in Jaback group contribution method.

A_{Cpi}	B_{Cpi}	C_{Cpi}	D_{Cpi}
−2.70	0.32	-9.70×10^{-6}	3.21×10^{-9}

Table S3. Heat capacity of solid ($C_{p,\,CrII}$ and $C_{p,\,CrI}$), liquid ($C_{p,\,l}$) and gaseous state ($C_{p,\,g}$) of $[N_{4444}][NTf_2]$.

Temperature (K)	$C_{p,\,CrII}$ (J K mol^{-1})	$C_{p,\,CrII}$ (J K mol^{-1})	$C_{p,\,l}$ (J K mol^{-1})	$C_{p,\,g}$ (J K mol^{-1})
100	201.95	/	/	229.46
123.15	257.18	/	/	277.07
143.15	303.74	/	/	317.31
163.15	349.23	/	/	356.74
183.15	393.65	/	/	395.37
203.15	436.99	/	/	433.24
223.15	479.26	/	/	470.35
243.75	521.68	/	/	507.09
263.15	/	624.76	/	542.41
283.15	/	668.11	/	577.38
298.15	/	702.07	/	603.17
303.15	/	713.67	/	611.69
323.15	/	761.43	/	645.34
343.15	/	811.41	/	678.36
363.95	/	865.72	/	712.06
383.15	/	/	999.44	742.59
403.15	/	/	1027.07	773.84
423.15	/	/	1054.11	804.53
443.15	/	/	1073.75	834.69
463.15	/	/	1094.46	864.34
483.15	/	/	1110.62	893.49
503.15	/	/	1123.61	922.18
523.15	/	/	1133.42	950.41
543.15	/	/	1140.06	978.21
568.15	/	/	1143.89	1012.38

Table S4. The polynomial parameters of the heat capacities of $[C_2mim][NTf_2]$.

Parameters	$C_{p,s}$ [a]	$C_{p,l}$ [b]	$C_{p,g}$ [c]
a_0	80.54	215.80	80.15
a_1	1.22	1.53	1.23
a_2	/	-1.65×10^{-3}	-9.05×10^{-4}
a_3	/	/	2.53×10^{-7}
R^2	0.997	0.999	0.999

[a] Reference 29; [b] Reference 30; [c] Reference 33.

Table S5. The polynomial parameters of the heat capacities of $[C_4mim][NTf_2]$.

Parameters	$C_{p,s}$ [a]	$C_{p,l}$ [b]	$C_{p,g}$ [c]
a_0	119.80	−80.22	99.20
a_1	1.17	3.59	1.34
a_2	/	-4.4×10^{-3}	-8.93×10^{-4}
a_3	/	/	2.22×10^{-7}
R^2	0.997	0.999	0.999

[a] Reference 32; [b] Reference 30; [c] Reference 33.

Table S6. The results of mass loss rate and $10^3|dm/dt|$ of $[N_{4444}][NTf_2]$ and glycerol.

	T (°C)	$10^3\lvert dm/dt\rvert$ (mg min^{-1})[a]	R^2	sd
$[N_{4444}][NTf_2]$	230	0.2970 ± 0.0213	0.9998	0.00010
	260	1.650 ± 0.0212	0.9999	0.00010
	290	8.40 ± 0.0226	0.9996	0.00410
	310	26.38 ± 0.0268	0.9998	0.00928
	330	77.82 ± 0.0280	0.9999	0.01105
	350	186.4 ± 0.4070	0.9988	0.20290
Glycerol	100	23.70 ± 0.110	0.9960	0.03046
	120	68.80 ± 0.130	0.9978	0.06490
	140	236.1 ± 0.078	0.9999	0.01266
	160	634.3 ± 0.080	0.9999	0.03047

Standard uncertainties (at 0.68 confidence level, k = 1) are u(T) = 0.586 K, u(m) = 8.7 μg.

[a] Expanded uncertainties (at 0.95 confidence level, k = 2).

Table S7. The values of $\ln(T^{0.5}|dm/dt|)$, T and $10^3 T^{-1}$ for $[N_{4444}]$ $[NTf_2]$ and glycerol.

	T (K)	10^3 T^{-1}	$\ln(T^{0.5}\|dm/dt\|)$ ($K^{0.5}$ mg min^{-1})	R^2	sd
$[N_{4444}][NTf_2]$	503.15	1.9875	−5.01 ± 0.00059	0.9983	0.3522
	533.15	1.8756	−3.27 ± 0.00055		
	563.15	1.7757	−1.61 ± 0.00052		
	583.15	1.7148	−0.45 ± 0.00050		
	603.15	1.6580	0.65 ± 0.00049		
	623.15	1.6048	1.54 ± 0.00047		
Glycerol	373.15	2.6799	−0.78 ± 0.00078	0.9977	0.3095
	393.15	2.5436	0.31 ± 0.00074		
	413.15	2.4204	1.57 ± 0.00071		
	433.15	2.3087	2.58 ± 0.00068		

Standard uncertainties (at 0.68 confidence level, k = 1) are u(T) = 0.586 K, u(m)=8.7 μg.

[a] Expanded uncertainties (at 0.95 confidence level, k = 2).

Table S8. The values of ΔH_{vap}, ΔH_{sub} and E_{coh} of $[N_{4444}][NTf_2]$.

Temperature (°C)	ΔH_{vap} (kJ mol^{-1})	ΔH_{sub} (kJ mol^{-1})	E_{coh} (kJ mol^{-1})
295	144.2	/	139.5
270	147.9	/	143.4
250	151.4	/	147.0
230	155.3	/	151.1
210	159.5	/	155.5
190	164.0	/	160.1
170	168.7	/	165.0
150	173.6	/	170.1
130	178.6	/	175.3
110	183.7	/	180.6
90.8	188.9	/	185.8
90	/	212.2	209.1
80	/	213.6	210.7
70	/	215.0	212.2
50	/	217.5	214.8
30	/	219.7	217.1
10	/	221.6	219.2
−10	/	223.3	221.1
−29.4	/	224.9	222.9
−30		225.8	223.7
−50	/	226.0	224.1
−70	/	226.1	224.4
−90	/	226.1	224.6
−110	/	226.0	224.7
−130	/	225.8	224.6
−150	/	225.5	224.5
−173.15	/	224.9	224.1

Table S9. The values of ΔH_{vap}, ΔH_{sub} and E_{coh} of $[C_2mim][NTf_2]$.

Temperature (°C)	ΔH_{vap} (kJ mol^{-1})	ΔH_{sub} (kJ mol^{-1})	E_{coh} (kJ mol^{-1})
124.35	122.0	/	118.7
104.35	124.5	/	121.3
84.35	127.1	/	124.1
64.35	129.8	/	127.0
44.35	132.7	/	130.1
24.35	135.7	/	133.2
2.40	139.0	/	136.7
−1.71	139.7	/	137.4
−1.73	/	161.5	159.3

Table S9 (Continued).

Temperature (°C)	ΔH_{vap} (kJ mol^{-1})	ΔH_{sub} (kJ mol^{-1})	E_{coh} (kJ mol^{-1})
−21.71	/	162.6	160.5
−41.71	/	163.6	161.6
−61.71	/	164.3	162.6
−81.71	/	165.0	163.4
−101.71	/	165.5	164.1
−121.71	/	165.9	164.7
−141.71	/	166.2	165.1
−153.15	/	166.4	165.4
−161.71	/	166.5	165.5
−181.71	/	166.6	165.9
−201.71	/	166.7	166.1
−221.71	/	166.8	166.4
−241.71	/	166.8	166.6
−243.71	/	166.8	166.6
−245.71	/	166.8	166.6
−247.71	/	166.8	166.6
−249.71	/	166.8	166.6
−251.71	/	166.8	166.7
−253.71	/	166.8	166.7
−255.71	/	166.8	166.7
−257.71	/	166.8	166.7
−259.71	/	166.8	166.7
−261.71	/	166.8	166.7
−262.71	/	166.8	166.7
−263.71	/	166.8	166.8
−264.71	/	166.8	166.8
−265.71	/	166.8	166.8
−266.71	/	166.8	166.8
−267.71	/	166.8	166.8
−268.71	/	166.8	166.8
−269.71	/	166.8	166.8
−270.71	/	166.8	166.8
−271.71	/	166.8	166.8
−273.15	/	166.8	166.8

Table S10. The values of ΔH_{vap}, ΔH_{sub} and E_{coh} of $[C_4mim][NTf_2]$.

Temperature (°C)	ΔH_{vap} (kJ mol^{-1})	ΔH_{sub} (kJ mol^{-1})	E_{coh} (kJ mol^{-1})
204.45	118.3	/	114.3
184.45	120.0	/	116.2
164.45	122.1	/	118.4
144.45	124.6	/	121.1
124.45	127.4	/	124.1
104.45	130.4	/	127.3
84.45	133.7	/	130.7
64.45	137.1	/	134.3
44.45	140.6	/	137.9
24.45	144.1	/	141.6
6.90	147.1	/	144.8
6.88	/	167.0	164.7
−12.85	/	167.7	165.6
−32.85	/	168.3	166.3
−52.85	/	168.9	167.0
−72.85	/	169.3	167.6
−92.85	/	169.7	168.2
−112.85	/	170.0	168.7
−132.85	/	170.3	169.1
−152.85	/	170.6	169.6
−172.85	/	170.8	170.0
−192.85	/	171.0	170.4
−212.85	/	171.3	170.8
−232.85	/	171.6	171.3
−252.85	/	171.9	171.8
−273.15	/	172.3	172.3

Table S11. The vapor pressures (P_{vap}) of $[N_{4444}][NTf_2]$ and glycerol.

	T (°C)	P_{vap} (Pa)	Ref
$[N_{4444}][NTf_2]$	230	0.209	This work
	260	1.20	
	290	6.26	
	310	20	
	330	60	
	350	146	
Glycerol	100	30	15
	120	90	
	140	320	
	160	980	

Table S12. The values of ΔS_{vap} and ΔG_{vap} of $[N_{4444}][NTf_2]$.

Temperature (°C)	ΔS_{vap} (J K^{-1} mol^{-1})	ΔG_{vap} (kJ mol^{-1})
295	177.6	43.3
270	182.8	48.6
250	190.8	51.6
230	198.4	55.4
210	206.9	59.5
190	216.4	63.7
170	226.9	68.2
150	238.2	72.8
130	250.4	77.7
110	263.4	82.8
90.8	277.1	88.0

Table S13. The values of ΔS_{sub} and ΔG_{sub} of $[N_{4444}][NTf_2]$.

Temperature (°C)	ΔS_{sub} (J K^{-1} mol^{-1})	ΔG_{sub} (kJ mol^{-1})
90	341.1	88.3
80	345.8	91.5
70	350.3	94.8
50	358.7	101.6
30	366.5	108.6
10	373.7	115.7
−10	380.7	123.1
−29.4	387.5	130.7
−30	391.1	130.7
−50	392.1	138.5
−70	392.7	146.3
−90	392.8	154.2
−110	392.2	162.0
−130	390.8	169.9
−150	388.3	177.7
−173.15	383.3	186.6

Table S14. The values of ΔS_{vap} and ΔG_{vap} of $[C_2mim][NTf_2]$.

Temperature (°C)	ΔS_{vap} (J K^{-1} mol^{-1})	ΔG_{vap} (kJ mol^{-1})
124.4	154.6	60.5
104.4	161.0	63.7
84.4	168.1	67.0
64.4	176.0	70.4
44.4	184.8	74.0

Table S14 (Continued).

Temperature (°C)	ΔS_{vap} (J K^{-1} mol^{-1})	ΔG_{vap} (kJ mol^{-1})
24.4	194.5	77.8
2.4	206.2	82.2
−1.7	208.5	83.1

Table S15. The values of ΔS_{sub} and ΔG_{sub} of [C_2mim][NTf_2].

Temperature (°C)	ΔS_{sub} (J K^{-1} mol^{-1})	ΔG_{sub} (kJ mol^{-1})
−1.8	289.2	83.1
−21.7	293.3	88.9
−41.7	297.1	94.8
−61.7	300.7	100.8
−81.7	303.9	106.8
−101.7	306.7	112.9
−121.7	309.3	119.1
−141.7	311.5	125.3
−153.2	312.7	128.9
−161.7	313.5	131.5
−181.7	315.0	137.8
−201.7	316.3	144.1
−221.7	317.3	150.5
−241.7	317.9	156.8
−243.7	318.0	157.5
−245.7	318.0	158.1
−247.7	318.1	158.7
−249.7	318.1	159.4
−251.7	318.2	160.0
−253.7	318.2	160.6
−255.7	318.3	161.3
−257.7	318.3	161.9
−259.7	318.4	162.6
−261.7	318.4	163.2
−262.7	318.4	163.5
−263.7	318.5	163.8
−264.7	318.5	164.1
−265.7	318.6	164.5
−266.7	318.6	164.8
−267.7	318.7	165.1
−268.7	318.7	165.4
−269.7	318.8	165.7
−270.7	318.9	166.1
−271.7	319.1	166.4

Table S16. The values of ΔS_{vap} and ΔG_{vap} of $[C_4mim][NTf_2]$.

Temperature (°C)	ΔS_{vap} (J K^{-1} mol^{-1})	ΔG_{vap} (kJ mol^{-1})
204.5	186.4	29.3
184.5	190.0	33.0
164.5	194.7	36.9
144.5	200.5	40.8
124.5	207.4	44.9
104.5	215.3	49.1
84.5	224.2	53.5
64.5	234.0	58.1
44.5	244.6	62.9
24.5	256.0	67.9
6.9	266.5	72.5

Table S17. The values of ΔS_{sub} and ΔG_{sub} of $[C_4mim][NTf_2]$.

Temperature (°C)	ΔS_{sub} (J K^{-1} mol^{-1})	ΔG_{sub} (kJ mol^{-1})
7.0	337.6	72.5
−12.9	340.2	79.2
−32.9	342.6	86.0
−52.9	344.9	92.9
−72.9	347.0	99.8
−92.9	349.0	106.8
−112.9	350.9	113.8
−132.9	352.8	120.8
−152.9	354.8	127.9
−172.9	357.0	135.0
−192.9	359.8	142.2
−212.9	363.5	149.4
−232.9	369.3	156.7
−252.9	380.5	164.2

Table S18. DTG onset temperatures (T_{onset}) and peak temperatures (T_p) value of $[N_{4444}][NTf_2]$.

β_H (°C min^{-1})	T_{onset} (°C)	T_p (°C)
0	368.5[a]	391.1[a]
5	379.3	402.6
10	387.7	412.2
15	393.7	419.9

[a] The T_{onset} and T_p at 0°C min^{-1} were derived from the polynomial.

Table S19. The values of k and $t_{1/2}$ at different temperatures of $[N_{4444}][NTf_2]$.

Temperature (°C)	k (h^{-1})	$t_{1/2}$ (h)
330	1.81×10^{-3}	382.03
335	2.71×10^{-3}	255.95
340	4.02×10^{-3}	172.60
345	5.92×10^{-3}	117.14
350	8.66×10^{-3}	79.99
355	1.26×10^{-3}	54.96
360	1.82×10^{-3}	37.99
365	2.62×10^{-2}	26.41
370	3.75×10^{-2}	18.46
375	5.34×10^{-2}	12.98
380	7.56×10^{-2}	9.17
385	0.11	6.52
390	0.15	4.65
395	0.21	3.34
400	0.29	2.41
405	0.40	1.75
410	0.55	1.27
415	0.75	0.93
420	1.00	0.68
425	1.70	0.50
430	1.85	0.37
435	2.49	0.28
440	3.33	0.21

Table S20. The E_a and R^2 obtained by FWO, KAS and Starink methods.

	FWO		KAS		Starink	
α(%)	E_a (kJ mol^{-1})	R^2	E_a (kJ mol^{-1})	R^2	E_a (kJ mol^{-1})	R^2
5	385.0	1.000	389.3	1.000	386.6	1.000
10	359.3	0.991	361.9	0.991	359.4	0.991
15	339.9	0.989	341.3	0.988	338.9	0.988
20	325.6	0.989	326.1	0.989	323.9	0.989
25	313.2	0.988	313.0	0.988	310.9	0.988
30	305.9	0.990	305.2	0.989	303.2	0.989
35	296.8	0.990	295.5	0.989	293.6	0.989
40	289.1	0.990	287.4	0.989	285.5	0.989
45	282.4	0.989	280.3	0.988	278.5	0.988
50	286.9	0.993	285.0	0.992	283.1	0.992
55	274.1	0.989	271.5	0.988	269.7	0.988
60	269.0	0.988	266.0	0.987	264.3	0.987
65	266.9	0.989	263.8	0.988	262.1	0.988
70	263.5	0.989	260.2	0.988	258.5	0.988
75	260.7	0.987	257.2	0.986	255.6	0.986
80	259.3	0.986	255.6	0.985	254.0	0.985
85	259.3	0.985	255.6	0.983	254.0	0.984
90	262.2	0.984	258.6	0.983	257.0	0.983

Notes and references for Supporting information

1 X. Zhao, H. Wu, M. Duan, X. Hao, Q. Yang, Q. Zhang and X. Huang, *Fluid Phase Equilib.*, 2018, **459**, 135.

2 S. Mena and G. Guirado, *J. Mol. Liq.*, 2020, **312**, 113393.

3 K. Noack, P. S. Schulz, N. Paape, J. Kiefer, P. Wasserscheid and A. Leipertz, *Phys. Chem. Chem. Phys.*, 2010, **12**, 14153-14161.

4 L. M. Ramenskaya, E. P. Grishina and N. O. Kudryakova, *J. Mol. Liq.*, 2020, **312**, 113368.

5 J. Kiefer, J. Fries and A. Leipertz, *Appl. Spectrosc.*, 2007, **61**, 1306-1311.

6 M. A. Assenine, B. Haddad, A. Paolone, S. A. Brandán, M. Goussem, D. Villemin, M. Boumediene, M. Rahmouni and S. Bresson, *J. Mol. Struct.*, 2021, **1232**, 130085.

7 X. Han, J. Ke, N. Suleiman, W. Levason, D. Pugh, W. Zhang, G. Reid, P. Licence and M. W. George, *Phys. Chem. Chem. Phys.*, 2016, **18**, 14359-14369.

8 S. P. Verevkin, D. H. Zaitsau, V. N. Emel'yanenko, R. V. Ralys, A. V. Yermalayeu and C. Schick, *Thermochim. Acta*, 2013, **562**, 84-95.

9 Y. U. Paulechka, G. J. Kabo and V. N. Emel'yanenko, *J. Phys. Chem. B*, 2008, **112**, 15708-15717.

10 K. G. Joback, Massachusetts Institute of Technology.

11 Y. Marcus, *Ionic liquid properties : from molten salts to RTILs*, Cham: Springer, Cham, 2016.

12 A. Loewenschuss and Y. Marcus, *J. Phys. Chem. Ref. Data*, 1987, **16**, 61-89.

13 P. Phang, D. Dollimore and S. J. Evans, *Thermochim. Acta*, 2002, **392-393**, 119-125.

14 G. A. B. Huimin Luo, Sheng Dai, *J. Phys. Chem. B*, 2008, **112**, 10077–10081.

15 G. P. Association, *Glycerine Producers' Association*, 1963.

16 J. P. Armstrong, C. Hurst, R. G. Jones, P. Licence, K. R. J. Lovelock, C. J. Satterley and I. J. Villar-Garcia, *Phys. Chem. Chem. Phys.*, 2007, **9**, 982-990.

17 E. Madelung, *Phys. Zs*, 1918, **19**, 524-533.

18 E. I. Izgorodina, U. L. Bernard, P. M. Dean, J. M. Pringle and D. R. MacFarlane, *Cryst. Growth Des.*, 2009, **9**, 4834-4839.

19 T. Ozawa, *Bull. Chem. Soc. Jpn.*, 1965, **38**, 1881-1886.

20 H. E. Kissinger, *Anal. Chem*, 1957, **29**, 1702-1706.

21 M. J. Starink, *Thermochim. Acta*, 1996, **288**, 97-104.

22 P. Ptáček, F. Šoukal, T. Opravil, J. Havlica and J. Brandštetr, *Powder Technol.*, 2011, **208**, 20-25.

23 Y. Xu and B. Chen, *Bioresource Technol.*, 2013, **146**, 485-493.

24 K. S. Quraishi, M. A. Bustam, S. Krishnan, M. I. Khan, C. D. Wilfred and J.-M. Lévêque, *J. Therm. Anal. Calorim.*, 2017, **129**, 261-270.

25 A. Ruvolo-Filho and P. S. Curti, *Ind. Eng. Chem. Res.*, 2006, **45**, 7985-7996.

26 L. Mu, J. Chen, H. Yin, X. Song, A. Li and X. Chi, *Bioresource Technol.*, 2015, **180**, 22-31.

27 S. Vyazovkin, *Int. J. Chem. Kinet.*, 1996, **28**, 95-101.

28 S. Vyazovkin and W. Linert, *Int. J. Chem. Kinet.*, 1995, **27**, 73-84.

29. Y. U. Paulechka, A. V. Blokhin, G. J. Kabo and A. A. Strechan, *J. Chem. Thermodyn.*, 2007, **39**, 866-877.

30. R. Ge, C. Hardacre, J. Jacquemin, P. Nancarrow and D. W. Rooney, *J. Chem. Eng. Data*, 2008, **53**, 2148-2153.

31. C. Červinka, M. Klajmon and V. c. Štejfa, *J. Chem. Theory Comput*, 2019, **15**, 5563-5578.

32. A. V. Blokhin, Y. U. Paulechka and G. J. Kabo, *Thermochimica acta*, 2006, **445**, 75-77.

33. Y. U. Paulechka, G. J. Kabo and V. N. Emel'yanenko, *J. Phys. Chem. B*, 2008, **112**, 15708-15717.